

RESEARCH ARTICLE | JUNE 21 2023

Inexpensive multi-plane particle image velocimetry based on defocusing: Proof of concept on two-component measurement

He Qichi (何启屹) ; Christopher Willman ; Richard Stone ; Benjamin A. O. Williams  *Physics of Fluids* 35, 067122 (2023)<https://doi.org/10.1063/5.0151952>View
OnlineExport
Citation

CrossMark

Articles You May Be Interested In

Defocus asymmetry in projection printing

Journal of Vacuum Science & Technology B: Microelectronics and Nanometer Structures Processing, Measurement, and Phenomena (November 1994)

Visualization of polymer interfaces by phase contrast ("defocus") electron microscopy

Journal of Applied Physics (August 2008)

Wafer flatness as a contributor to defocus and to submicron image tolerances in step-and-repeat photolithography

Journal of Vacuum Science & Technology B: Microelectronics Processing and Phenomena (January 1987)

Inexpensive multi-plane particle image velocimetry based on defocusing: Proof of concept on two-component measurement

Cite as: Phys. Fluids **35**, 067122 (2023); doi: [10.1063/5.0151952](https://doi.org/10.1063/5.0151952)

Submitted: 26 March 2023 · Accepted: 5 June 2023 ·

Published Online: 21 June 2023



View Online



Export Citation



CrossMark

Qichi He (何启焜),  Christopher Willman,  Richard Stone,  and Benjamin A. O. Williams^{a)} 

AFFILIATIONS

Department of Engineering Science, University of Oxford, Oxford OX1 3PJ, United Kingdom

^{a)} Author to whom correspondence should be addressed: ben.williams@eng.ox.ac.uk

ABSTRACT

This paper presents a method for simultaneous particle image velocimetry (PIV) on parallel planes offset in depth. The method places images from two planes onto a different half of a camera sensor by using image splitting optics with variable optical path lengths. A shallow depth of field is achieved to ensure only one plane is in focus on each half of the sensor. Without needing additional lasers, the method is designed as an inexpensive means to increase the number of measurement plane(s) of single/multi-plane PIV setups and can be combined with existing plane discrimination approaches such as polarization and wavelength. The method is useful for studying instantaneous flow correlations on different planes while retaining high in-plane spatial resolution of typical planar PIV measurement. The measurement uncertainty caused by crosstalk from out-of-focus images is discussed. Experimental results from a laminar flow rig test indicate that the average measurement error of each velocity component is lower than 0.1 pixels per time step, with a 20 mm plane separation in depth and a $35 \times 54 \text{ mm}^2$ field of view. As an application with varying background scatter and out-of-plane flow motions, in-cylinder flow measurements in an optically accessible internal combustion engine were performed on two swirl planes simultaneously. Characteristics of the proposed method performing stereoscopic PIV measurements will be studied in future.

© 2023 Author(s). All article content, except where otherwise noted, is licensed under a Creative Commons Attribution (CC BY) license (<http://creativecommons.org/licenses/by/4.0/>). <https://doi.org/10.1063/5.0151952>

I. INTRODUCTION

Flow field velocity measurement underpins fluid mechanics research. To quantify the instantaneous velocity field within a plane, particle image velocimetry (PIV) is a widely adopted optical technique.¹ In a PIV experiment, tracer particles are seeded into and move with the flow. By performing cross-correlation in discrete subregions (called interrogation windows) of an image pair, the local flow velocity at each window can be acquired based on the known time difference between the two images, the statistical displacement of the particles within the window in the unit of pixel, and the local pixel to mm ratio. The planar PIV technique can also recover three-component (3C) velocity measurement with two cameras in a stereoscopic configuration.² However, for turbulent flows in which flow field structures are highly three-dimensional (3D), typical single-plane techniques cannot provide essential out-of-plane information. Much effort has been made to extend PIV to 3D velocity measurement. One such approach is scanning PIV.^{3–5} Although it is conceptually straightforward, the sequential nature of scanning PIV may limit its ability to capture the instantaneous fluctuations of highly turbulent flows.

Another common method for 3D flow measurement is tomographic PIV. With multiple cameras simultaneously taking images from different perspectives, 3D particle locations within the volume of interest are reconstructed.^{6,7} The application of tomographic PIV is limited by the spatial resolution it can achieve, since the reconstruction accuracy drops with increasing seeding density (i.e., number density of PIV particles per image, which determines the achievable minimum size of the interrogation windows). Generally, the spatial resolution can be increased by using more cameras, which can be difficult when optical access is limited, not to mention the high cost.

To acquire more out-of-plane information, while maintaining high in-plane spatial resolution of the measured velocity field, a common practice is to perform simultaneous multi-plane PIV. Conventionally, measurement planes are distinguished by different laser polarization directions or/and laser wavelengths.^{8–10} An advantage of the polarization and wavelength methods is that the measurement planes can be closely spaced, which allows the complete velocity gradient tensor to be measured within a plane. However, the number of measurement planes is limited by the wavelength/polarization

differences of the laser sheets. Assuming perfectly orthogonal linear polarizations can be achieved (which is questionable in practical engineering applications requiring optical access windows where stress induced birefringence is unavoidable), further increasing the number of measurement planes means introducing more laser sheets with different wavelengths, which is costly and adds experimental complexity. To the best of the authors' knowledge, by employing the polarization/wavelength approach, quad-plane PIV¹⁰ is state-of-the-art.

We present a multi-plane PIV method based on image splitting and defocusing. By using a non-polarizing beam splitter and mirrors with adjustable optical path lengths, each half of a camera sensor is focused to a different depth plane. With a shallow depth of field, the overlapping image that is not in-focus is significantly defocused. The in-plane spatial resolution of the measurement does not need to be compromised for measurement accuracy, compared to 3D PIV techniques. As an inexpensive and compact add-on, the image splitting optics design can be used alone or combined with the polarization/wavelength method, to increase the number of the measurement plane (s) of single/multi-plane PIV setups, while retaining the high in-plane spatial resolution characteristic of planar PIV measurement. In addition to cross-correlation-based measurements, we also note the possibility of extending our method to facilitate 3D particle tracking velocimetry (PTV),^{11,12} such as measurements in multiple 3D thin sub-volumes with a distinct separation.

The purpose of this paper is to provide a proof-of-concept evaluation of this novel multi-plane PIV method. The design and working principle are presented in Sec. II. The measurement error caused by crosstalk from out-of-focus images is analyzed in Sec. III, which is built upon the measurement results from a laminar flow field generated in a lab flow rig. In Sec. IV, simultaneous two-plane PIV is performed in an optically accessible internal combustion engine, as an application of the technique in a practical device with varying background signals and out-of-plane flow motions.

II. METHODOLOGY

A. Image splitting configuration

Figure 1 presents the image splitting optics design. To allow images from two parallel depth-offset planes to be focused on a single camera sensor, a 2-in. 50/50 non-polarizing beam splitter (Thorlabs

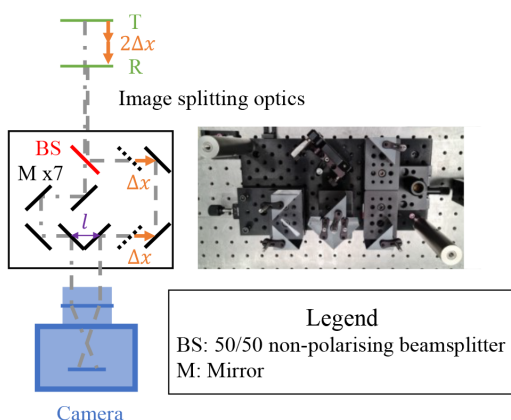


FIG. 1. Image splitting optics.

BSW42-532) is used to split scattered light from the two planes into two paths, namely, the transmitted-side path (T) and the reflected-side path (R). By using multiple mirrors, the light traveling along each path is directed to a different half of the camera sensor. Since light from either plane is 50/50 split into the two paths without bias, each half of the camera sensor receives light from both planes. In order to distinguish images from the two planes, the optical path lengths of the two paths can be adjusted independently. Although both optical paths share the same camera lens and image distance, by adjusting the positions of the mirrors (Δx in Fig. 1), the two parallel planes can be placed at different depths along the optical axis and have an adjustable separation ($2\Delta x$ in Fig. 1). Therefore, for either side of the camera sensor, the image from one plane is in-focus, while the other plane's image is out-of-focus. By using a large aperture camera lens ($f = 85 \text{ mm}$, $f/2$, in this paper), a shallow depth of field is achieved.

A 50/50 non-polarizing beam splitter (Edmund Optics 35959) is used to split a pair of PIV laser beams into two pairs. In order to control the widths of the laser illuminated regions on the measurement planes such that the in-focus images from both sides do not overlap, the laser sheets should travel vertically, instead of on the same horizontal plane where the image splitting optics is placed. In an experimental setup where optical access is limited and the laser sheets cannot be sent vertically, two blocking screens can be used to narrow the illuminated region seen by the camera sensor (Sec. III A), or the image splitting optics can be arranged to split the images in the vertical direction of the sensor.

Due to image overlapping, the maximum width of the field of view on the two measurement planes is affected by the distance (l in Fig. 1) between the centers of the two mirrors closest to the camera lens. That distance determines how far the two images on each side are separated. In this paper, since $35 \times 35 \text{ mm}^2$ prism mirrors (Edmund Optics 49-406) are used, the width of the field of view is set to be 35 mm, the maximum with this setup.

The proposed image splitting-based PIV method can be extended to stereoscopic measurement. As shown in Fig. 2, the object planes of the transmitted-side and the reflected-side images have the same working distance to the camera lens. Therefore, the Scheimpflug principle is valid for each side of the image, with each side sharing the same working distance, lens plane, and image plane. Characteristics of the proposed method performing stereoscopic PIV measurement will be studied in future.

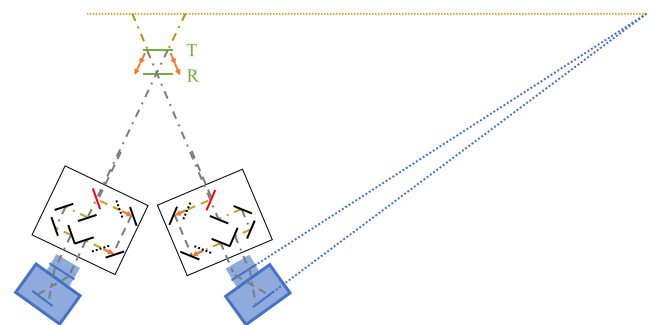


FIG. 2. Two-plane stereoscopic PIV based on the proposed image splitting configuration.

B. Depth of correlation

The depth of correlation concept originates from microscopic PIV (μ PIV), where generally the thickness of the volume of interest is smaller than the thickness of a laser sheet (~ 0.5 mm), and the entire flow volume is inevitably illuminated.^{13,14} Olsen and Adrian¹³ defined the depth of correlation parameter as twice the distance from the object plane to the nearest plane in which a particle image becomes sufficiently defocused to no longer contribute significantly in the PIV cross-correlation process. After making approximations, such as modeling an optical system as a single thin lens, depth of correlation may be calculated.^{13,15,16} Inevitably, in many μ PIV experiments, a deviation of the actual depth of correlation from its theoretically predicted value can be expected.¹⁴

The larger spatial scale involved in macroscopic PIV enables us to selectively choose a set of planes to illuminate, instead of mitigating against volumetric illumination as in most μ PIV experiments. In macroscopic multi-plane PIV, only discrete classes of defocused particle images would appear, instead of a continuous range of defocused images as in μ PIV. By leveraging a shallow depth of field, the interference from the out-of-focus images reduces drastically as the out-of-focus plane is further away from the plane of focus. In μ PIV, it is assumed that velocity variation along the depth direction is small that the effect of the defocused particles on the PIV cross-correlation process is “nudging” the correlation peak of the in-focus particles. In macroscopic PIV, the “correct” correlation peak produced by the in-focus particles and the “wrong” correlation peak produced by the defocused particles can be at any location in the correlation map, depending on the flow field. Therefore, the characterization of crosstalk between in-focus and defocused particles in macroscopic PIV needs to consider different combinations of correct and wrong peak locations.

III. CROSS-TALK ANALYSIS

A laminar flow rig was assembled, for a detailed investigation of the various types of measurement uncertainty caused by crosstalk from out-of-focus images.

A. Experimental setup

Figure 3 presents the setup of the laminar flow rig test. A pair of laser beams from a dual-cavity Nd:YAG laser (Gemini 200-15, New

Wave Research) was formed into a pair of laser sheets, illuminating the central plane of a rectangular section perspex tube (42×36 mm²). Developing laminar air flow ($Re_h = 160$) was generated by a flow straightener with circular microchannels (ϕ 0.85 and 1 mm spacing between each channel center). The air flow was seeded with di-ethyl-hexyl-sebacate (DEHS) particles (~ 0.4 μ m mean diameter), generated by a LaVision aerosol generator. The flow rig can be placed horizontally or vertically to generate flows with different directions. As will be discussed later, measurement uncertainties of the horizontal (u) and vertical (v) components of flow velocity are different, due to the characteristic shapes of the out-of-focus particle images. PIV images were taken by an Imperx B1621 double-frame CCD camera. A large aperture camera lens ($f = 85$ mm, $f/2$) was used to achieve a shallow depth of field. As discussed in Sec. II, since the laser sheets traveled on the same horizontal plane as the image splitting optics, two blocking screens were used to narrow the illuminated region seen by the camera sensor. The field of view on each side of the image is 35×54 mm².

To evaluate crosstalk between the in-focus images and the out-of-focus images at different plane separations, the PIV measurement results of in-focus images are compared to the results of “two-plane” images, which were generated by numerically adding in-focus images with out-of-focus images. Different plane separations were achieved by translating the mirrors on the transmitted and the reflected optical paths of the image splitting setup (indicated by arrows in the image splitting optics drawing in Fig. 3). Cross-talk at different plane separations is studied, respectively, on the transmitted-side and the reflected-side image, since the out-of-focus particles have different shapes and degrees of defocus on the two sides.

Table I summarizes the variables in the test. For the transmitted-side and the reflected-side image independently, 250 image pairs were collected at every combination of the test variables listed. In an actual PIV measurement, the laser pulse delay time dt within an image pair is fixed. Here, controlling dt is used to simulate flow fields with different flow velocities, while the laser energy and the particle seeding density remain the same. By numerically adding in-focus images with out-of-focus images having different velocities, different combinations of locations of the correct and wrong correlation peaks can be simulated.

PIV vector calculation was performed with a Matlab toolbox PIVlab (v2.56).¹⁷ A window deformation-based multi-pass algorithm was applied, with a modification of the correlation peak search procedure to prevent outliers, which is discussed in detail in Sec. III C 2. Decreasing interrogation windows from 96×96 to 64×64 pixels² with a 50% overlap were used, resulting in a vector spacing of 1.4 mm. Here, the final interrogation window size was determined so that the particle image density is about 30 particles per final interrogation

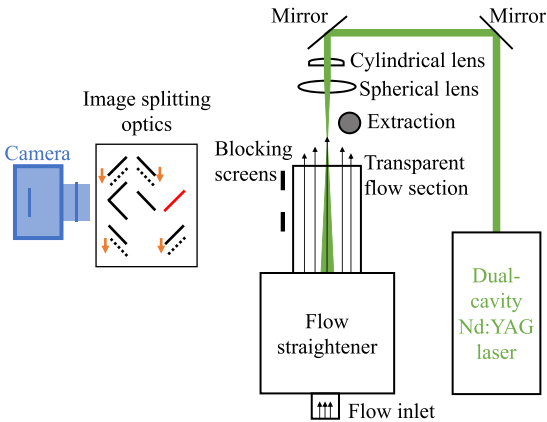


FIG. 3. Experimental setup of the laminar flow rig test (horizontal flow direction).

TABLE I. Summary of the test variables in the laminar flow rig test.

Flow direction	Plane separation (mm)	dt (ms) ^a
Horizontal	0 (in-focus)	2.71
	10	2.32
	15	1.94
	20	1.55
	25	0.19

^aLaser pulse delay time within an image pair.

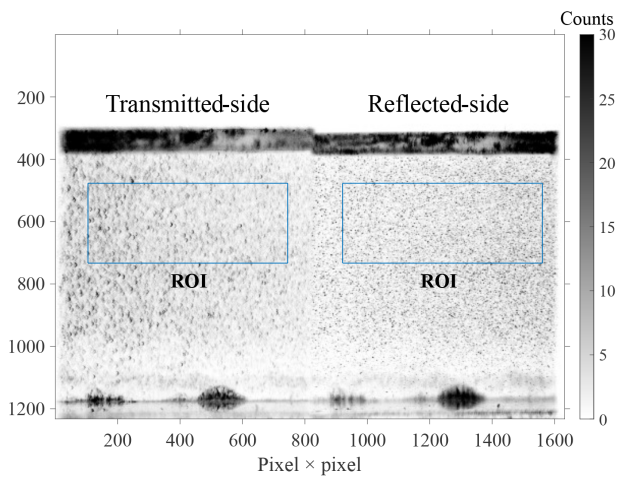


FIG. 4. An example of raw images (black and white inverted) in the horizontal flow test, overlaid with rectangles indicating the PIV regions of interest (ROI). In this image, the reflected-side image is in-focus, while the transmitted-side image is defocused, with a 15 mm plane separation. The horizontal bar along ~ 340 pixels is the scatter of the flow section wall.

window, which is similar to the one in the engine flow measurements (Sec. IV). The PIV regions of interest are indicated in Fig. 4. The characteristics of the in-focus/out-of-focus particle images are discussed next.

B. The optical characteristics of the split images

The degree of defocus of particles at different plane separations largely determines measurement uncertainty. Figure 5 shows examples of in-focus and defocused particle images in the PIV regions of interest. There are several observations we can make. First, the out-of-focus particles have elliptical shapes, looking like arcs. This is due to each optical path using a half of the camera lens for imaging. Because the shape of the particle images largely determines the shape of the PIV cross-correlation peak, an asymmetric particle shape would result in the horizontal and vertical component of velocity having different extents of crosstalk even at the same plane separation. Second, asymmetric defocus along the optical axis exists in either-side image, and it is more noticeable in the reflected-side image. In the reflected-side image, it can be noticed that when the out-of-focus particles are closer to the camera (i.e., the direction of the black dash arrow), the defocused particle images tend to have a distinct sharp-edged pattern, with intensity concentrated at their edges. The diffuse pattern on the other

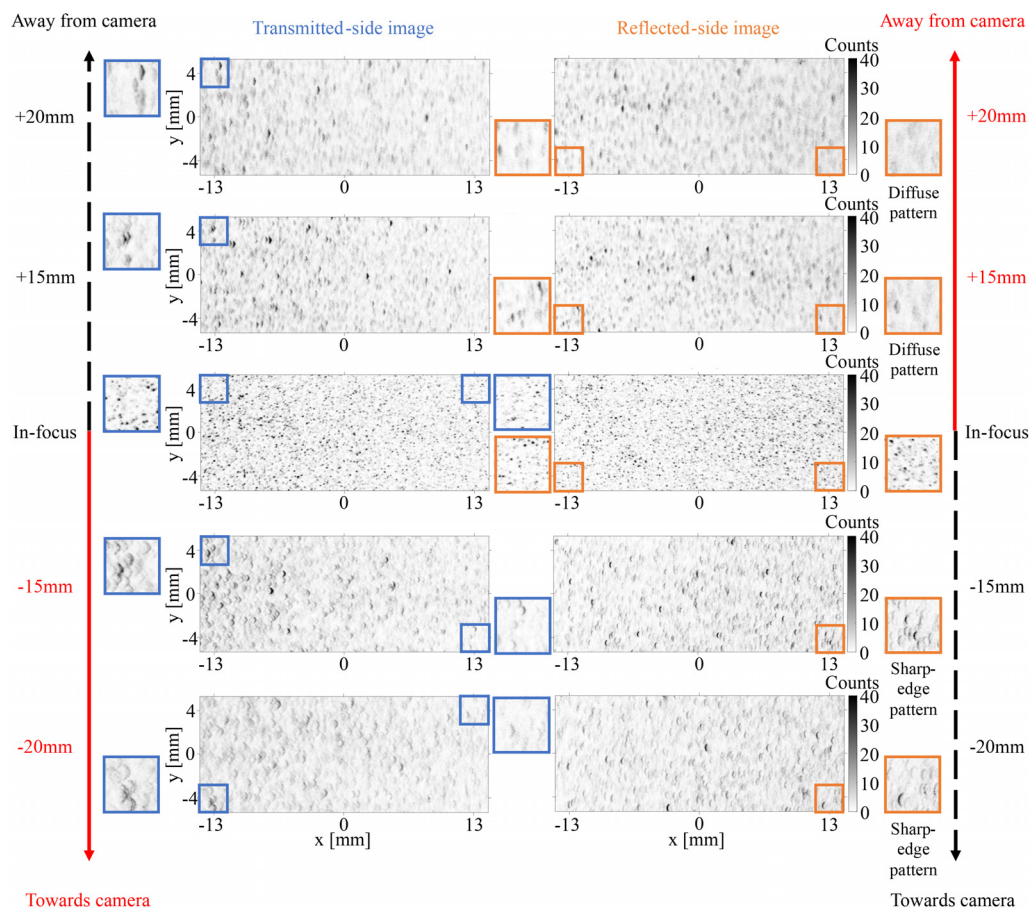


FIG. 5. Examples of raw images (black and white inverted) in the PIV regions of interest.

side of the plane of focus (i.e., the direction of the red solid arrow) is preferred, because diffuse particle images with spread intensity result in less sharp correlation peaks with lower height, which is beneficial for reducing crosstalk. This would be due to the asymmetry of optical aberration behind and in front of the plane of focus. Therefore, throughout this paper, the object plane configuration has been chosen such that the transmitted-side measurement plane is further away from the camera lens (as it is shown in Fig. 1). In other words, the out-of-focus images on the side of the red solid arrows are the out-of-focus images used for data analysis.

Third, it is also observable that the shapes of the defocused particle images are changing at different horizontal locations. It might be because for those particles horizontally far away from the optical axis, the incident angle of light is large, leading to aberrations that are made worse due to each optical path using only a horizontal half of the camera lens. The extent of such non-uniformity of defocusing might change if a different camera lens is used. In the measurement uncertainty analysis in Sec. III C, crosstalk at different horizontal locations will be discussed.

C. Uncertainty sources

Figure 6 summarizes the three types of measurement crosstalk caused by the out-of-focus particles. In μ PIV, velocity variation along the out-of-plane direction is assumed to be small, so that the correct and wrong correlation peaks “merge” into one, resulting in a mix peak biased toward the wrong peak (case 1). The effect of this kind of crosstalk has previously been modeled based on the curvature difference of the in-focus and out-of-focus correlation peaks.

In macroscopic PIV, the in-focus and out-of-focus particles could have very different velocities, such that a large range of locations for the correct and wrong peaks could occur. If bright/saturated out-of-focus particles exist within the interrogation window, a wrong

correlation peak with a large height could be generated, so that a conventional correlation peak search routine based on maximum peak height search would pick the wrong peak (case 2). Here, a cross-correlation peak search routine based on peak curvature is proposed and validated to prevent this issue. However, even if the correct correlation peak can be distinguished, its shape is still inevitably changed due to the interfering signal caused by the defocused particles, having an impact on sub-pixel displacement estimation (case 3). The three cases will now be discussed in detail.

1. Correlation peaks merging

Uncertainty caused by peaks merging has been extensively discussed and analyzed in μ PIV. The measured velocity can be seen as a weighted average of the velocities at different depths

$$u_0 = \frac{\int u(z)W(z)dz}{\int W(z)dz}, \quad (1)$$

in which $W(z)$ is a weighting function, quantifying the relative contributions of PIV particles at different depths. Bourdon *et al.*¹⁸ proposed a method to experimentally measure the weighting function. It starts by recognizing that the component of the overall correlation function related to the displacement of the particles is composed of the summation of individual correlation functions at each depth in the flow. In our case, finite depth is involved, and the correlation function R_D can be written as follows:

$$\langle R_D \rangle = \sum_{k=1}^n \langle R_D \rangle_k. \quad (2)$$

The overall measured velocity is the location s_0 where the slope of the overall correlation function is zero,

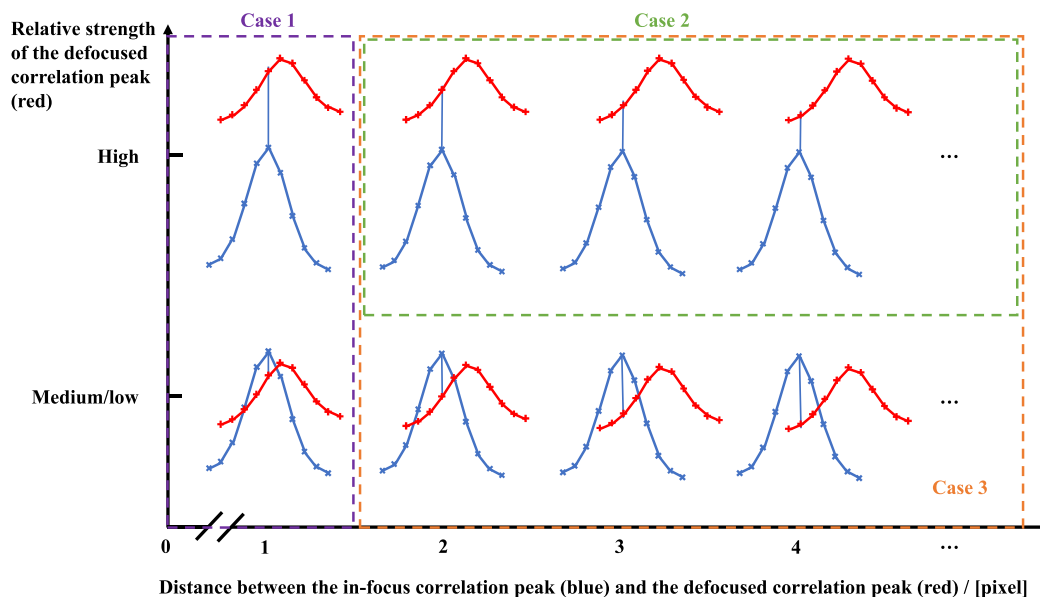


FIG. 6. A principle sketch of the three types of measurement crosstalk (color online). Case 1: the correct and wrong correlation peaks merge; case 2: the wrong correlation peak has a larger height, leading to the PIV algorithm choosing the wrong peak; and case 3: the shape of the correct peak is changed, resulting in measurement uncertainty in terms of sub-pixel displacement estimation.

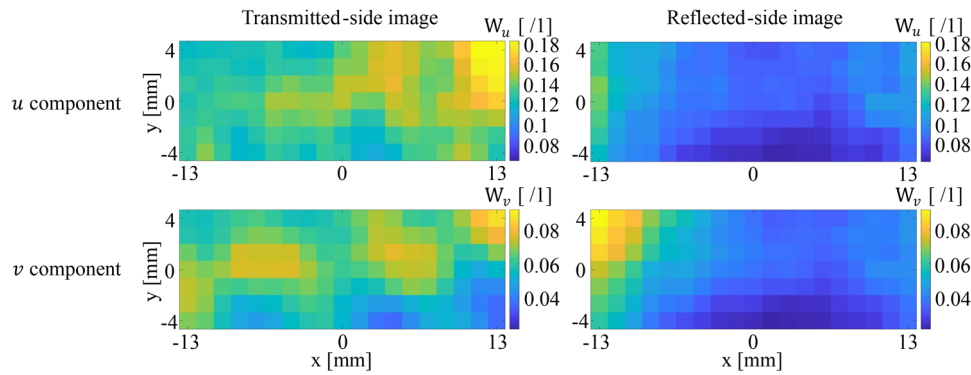


FIG. 7. The weighting functions in the PIV regions of interest, at a 15 mm plane separation. Note that the defocused particles closer to the center of the camera sensor have larger weights. The colorbar scales of the u and v component are different, due to the non-circular shapes of the defocused particle images. The weighting functions are calculated based on 250 images.

$$\frac{\partial \langle R_D \rangle}{\partial \mathbf{s}}(\mathbf{s}_0) = \sum_{k=1}^n \frac{\partial \langle R_D \rangle_k}{\partial \mathbf{s}}(\mathbf{s}_0) = 0. \quad (3)$$

By assuming that the location of the peak of each individual correlation differs from \mathbf{s}_0 by some small distance $\Delta \mathbf{s}_k$, the slope of each individual correlation function at the location \mathbf{s}_0 can be approximated by taking a Taylor series expansion around the location of each individual correlation peak

$$\begin{aligned} \frac{\partial \langle R_D \rangle_k}{\partial \mathbf{s}}(\mathbf{s}_0) &= \frac{\partial \langle R_D \rangle_k}{\partial \mathbf{s}}(\mathbf{s}_0 - \Delta \mathbf{s}_k) \\ &+ \frac{\partial^2 \langle R_D \rangle_k}{\partial \mathbf{s}^2}(\mathbf{s}_0 - \Delta \mathbf{s}_k) \Delta \mathbf{s}_k. \end{aligned} \quad (4)$$

The first term on the right-hand side of Eq. (4) is zero, because $\mathbf{s}_0 - \Delta \mathbf{s}_k$ is the location of the peak of each individual correlation. Substituting Eq. (4) into Eq. (3) leads to

$$\begin{aligned} \frac{\partial \langle R_D \rangle}{\partial \mathbf{s}}(\mathbf{s}_0) &= \sum_{k=1}^n \frac{\partial^2 \langle R_D \rangle_k}{\partial \mathbf{s}^2}(\mathbf{s}_0 - \Delta \mathbf{s}_k) \Delta \mathbf{s}_k = 0 \\ &= \sum_{k=1}^n W(z_k) \Delta \mathbf{s}_k = 0. \end{aligned} \quad (5)$$

Therefore, Bourdon *et al.*¹⁸ proposed that, by measuring the curvature at the peak of the individual correlation function, the relative contribution of particles at each individual depth can be quantified.

In this test, the transmitted-side and the reflected-side images were divided into 64×64 windows with a 50% overlap. The auto-correlation function of each window has a peak at the center. In our case, because the out-of-focus particle images have elliptical shapes, instead of being symmetric “circles” as in μ PIV, the curvature evaluation was performed separately on the x and y axes. Two Gaussian functions were fitted, respectively, on the central row and the central column of the auto-correlation function of each window. Curvatures were then calculated based on the fitted functions. For each interrogation window, the average curvatures calculated based on 250 images were used to calculate the weighting functions.

Figure 7 shows the weighting functions calculated in the PIV regions of interest at the 15 mm plane separation. Differences in the weighting functions across the sensor width can be noticed: the out-of-focus particles generally have larger contributions in the central region of the camera sensor, due to the change of the defocused particle image shape at different horizontal locations (first shown in Fig. 5).

Figure 8 plots the weights of the defocused particle images in each interrogation window at different plane separations. Several

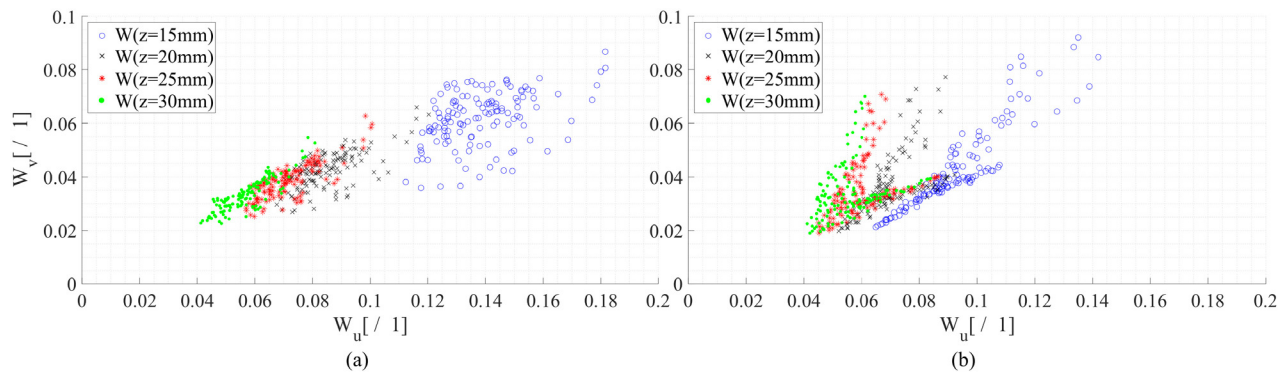


FIG. 8. The weighting functions in the PIV regions of interest of the: (a) transmitted-side image and (b) reflected-side image. Each scatter point corresponds to one interrogation window.

observations need to be made. First, even at the same plane separation, difference in the weighting functions of different interrogation windows can be noticed (as visualized in Fig. 7). Second, the relative contribution of the defocused particles on the u component of velocity is larger, because of the characteristic arc shape of the defocused particle images. Third, as the plane separation further increases, the reduction of the weights becomes slower. This indicates a limit of minimum crosstalk caused by “peaks merging.” The limit is mostly dependent on the aperture of the optical system. However, since the weighting function calculation is based on the assumption that the correct and wrong correlation peaks are close to each other ($\Delta s_k \rightarrow 0$), the absolute measurement error caused by “peaks merging” is actually limited. This will be shown by the PIV measurement results in Sec. III C 3.

2. Correlation peak search based on peak shape: Outlier removal

In PIV, seeding particles that have a diameter of the order as the wavelength of the incident light are used, so that strong Mie scattering is used for particle detection. The Mie signal is proportional to the square of the particle diameter. PIV particles generated by practical seeding devices have a certain size distribution, instead of being monodisperse. Therefore, in PIV images, some particles are brighter than others due to their sizes. The spatial distribution of the laser sheet intensity is another source of the brightness difference of particles, because a laser sheet has a finite thickness, generally having the peak intensity at the center. As can be noticed in Fig. 5, although most of the defocused particles have weak intensities, some bright blurry particles still occasionally appear.

Generally, a PIV algorithm determines the statistical displacement of particles by searching for the maximum of the cross-correlation function. However, as shown in Fig. 6, the correlation peak produced by bright out-of-focus particles can occasionally have a larger height, resulting in outliers occurring.

Inspired by the curvature difference of the correlation peaks produced by the in-focus and the out-of-focus particles, we propose a correlation peak search routine taking advantage of the correlation peak shape difference. When searching for the correlation peak, instead of directly choosing the peak with the maximum height, the location having the maximum directionally averaged second derivative is picked,

$$(x_c, y_c) = \operatorname{argmax} \frac{\frac{\partial^2 R(x_i, y_i)}{\partial x^2} + \frac{\partial^2 R(x_i, y_i)}{\partial y^2}}{2}. \quad (6)$$

Then, the pixel (x_p, y_p) having the maximum correlation function value among the neighboring pixels of (x_c, y_c) is chosen to be the correlation peak. Sub-pixel estimation is then applied.

To test the effectiveness of the proposed sharp peak search procedure, the laminar flow test data from an extreme test point are used here. The in-focus image pairs have a laser pulse delay time $dt = 2.71$ ms, corresponding to a particle displacement of ~ 8 pixels. The out-of-focus image pairs have $dt = 0.19$ ms, corresponding to a particle displacement of ~ 0 pixel. The reason for using this test condition is that, in this paper, a cyclic FFT-based cross-correlation algorithm is used to calculate the cross-correlation functions. Cyclic means that the cross-correlation is computed as if the two interrogation windows were repeated in 2D space. This is a standard operation in PIV processing. The cyclic FFT-based cross-correlation introduces a bias to

the weightings of the cross-correlation function at different locations within the interrogation window. The center of the window has the largest weight, with reducing weightings as the particle displacement is increased. That means a wrong correlation peak produced by bright out-of-focus particles has an even larger height if it corresponds to a small particle displacement. Among all of our test points, it is mostly likely for this test point to have case 2 error; therefore, we have chosen it to validate the effectiveness of our proposed method. To be specific, in this test point, due to certain bright out-of-focus particles, a PIV algorithm based on the conventional highest peak search routine could output 0 pixel instead of 8 pixels as the measurement result, generating outliers.

Figure 9 presents the percentages of outliers out of 250 image pairs, to compare the effect of the proposed sharp peak search routine with the conventional highest peak search routine. Here, the conventional highest peak search routine is also applied to image pairs pre-processed with a high-pass filter, which is a typical image filter for removing low-frequency noise. The high-pass filter used in this test was that implemented in the PIVlab package. It subtracts the images' low-frequency content generated from a 2D Gaussian smoothing kernel (15×15 pixels in this test). We can conclude that the high-pass filter is able to help with reducing the outlier occurrence, and the proposed sharp peak search routine can more effectively prevent outliers. In this case, it can be noticed that the outlier occurrence is actually not frequent even when the proposed sharp peak search routine or high-pass filtering is not applied. It is expected that in experiments where solid PIV particles are used and particle clumps exist, the proposed sharp peak search routine would be more helpful.

Throughout this paper, the PIV vector calculations of all two-plane image pairs, including the numerically added ones and the simultaneous ones, were performed based on the proposed sharp peak search routine.

3. Correlation peak shape change

With the presence of the defocused particles, the shape of the correct correlation peak of the in-focus particles would inevitably change, resulting in uncertainty in terms of sub-pixel displacement estimation. The influence of the peak shape change would largely depend on the slope of the wrong correlation peak at the location where the correct peak is. The absolute correlation function values of the two peaks would also make a difference. It is not easy to accurately model the measurement uncertainty caused by peak shape change, due to camera noise, the non-uniform distribution of PIV particles within the flow, and the brightness difference of the particles. However, it is expected that the influence of the peak shape change would reach the maximum when the correct peak is located at the steepest part of the wrong peak, and then reduce as the correct peak approaches the margins of the wrong peak. In this test, in-focus image pairs having the same $dt = 2.71$ ms were numerically added with different out-of-focus image pairs having different dt s, to generate two-plane image pairs with different combinations of correct and wrong peaks' locations. For each combination, 250 image pairs are analyzed. Considering the characteristic arc shape of the defocused particle images, the measurement uncertainty is evaluated separately on the horizontal and vertical component of velocity, by switching the orientation of the flow rig. It is noted that throughout this section, no vector post-processing was applied to the measured velocity fields.

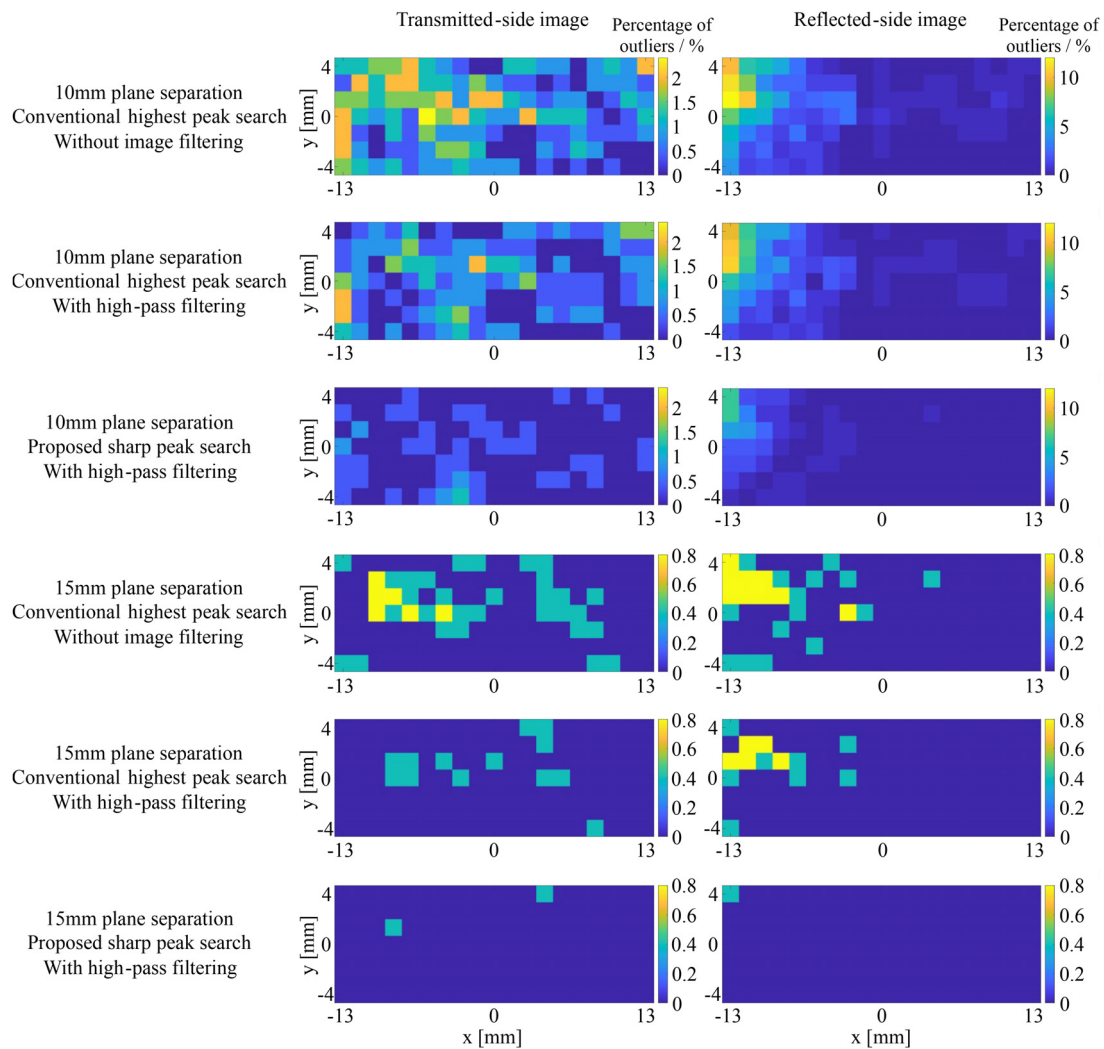


FIG. 9. Percentages of measurement outliers: comparison between the conventional highest peak search routine and the proposed sharp peak search routine (test condition: in-focus image pairs have a particle displacement of ~ 8 pixels, out-of-focus image pairs have a particle displacement of ~ 0 pixel). The effect of high-pass filtering is also compared. Note the different colorbar scales used for different plane separations and the different sides of image.

Figure 10 shows the average velocity fields of the in-focus image pairs. To examine the measurement uncertainty, the flow profiles of the three marked regions in Fig. 10 are analyzed. Two regions are investigated for the horizontal flow, in order to look into the difference caused by the change of the defocused particle image shape at different horizontal locations (first shown in Fig. 5). As an example, Fig. 11 shows the average flow profiles of the in-focus image pairs, the defocused image pairs, and the numerically added two-plane image pairs in region 1 of the reflected-side image at 15 mm plane separation. The different Δt s of the defocused image pairs were chosen so that the velocity difference between the correct velocity and the wrong velocity includes: ~ 1 pixel per time step (green, diamond), ~ 2 pixels per time step (black, cross), and ~ 3 pixels per time step (cyan, circle). As the difference between the correct velocity and the wrong velocity increases, the bias of the measurement result first increases and then reduces. This could

be explained by: when the distance between the peaks is ~ 2 pixels, the correct correlation peak is at the highest gradient part of the wrong correlation peak, which can be visualized in Fig. 6. In the cross-correlation domain, if we assume that the focused particles and defocused particles have negligible correlations (and also neglect noise), the correlation function of the two-plane image is the linear sum of the focused and defocused correlation functions. When the focused correlation peak is at the highest gradient of the defocused correlation peak, the defocused correlation signal would give the greatest disturbance to the focused peak signal. Because a PIV algorithm uses the neighboring pixel readings of the focused peak to interpolate for sub-pixel displacement, the greatest disturbance to the focused peak signal also means the greatest disturbance to the sub-pixel displacement estimation.

To closely inspect the measurement errors, Figs. 12 and 13 plot the average absolute errors in the three regions at the 15 and 20 mm

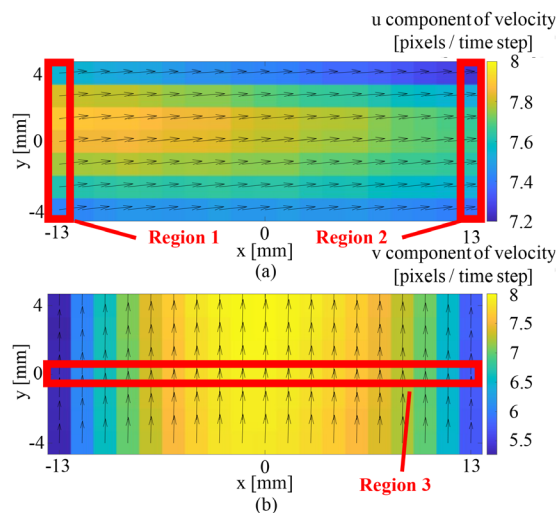


FIG. 10. The average velocity fields of 250 in-focus image pairs of: (a) the horizontal flow and (b) the vertical flow. Note the different colorbar scales.

plane separations. An obvious difference in the measurement error of regions 1 and 2 can be observed in the reflected-side image, but not in the transmitted-side image. This disparity could be understood by reference back to Fig. 5 in which the asymmetric defocus effect on the reflected-side image is more noticeable. Overall, when the correct correlation peak is about 2 pixels away from the wrong peak, the measurement bias reaches the maximum, corresponding to the steepest part of the wrong peak. At 15 mm plane separation, the average absolute error of either the horizontal or the vertical component of velocity is smaller than 0.2 pixels per time step; at 20 mm plane separation, the average absolute error of either the horizontal or the vertical component of velocity is smaller than 0.1 pixels per time step. For a specific

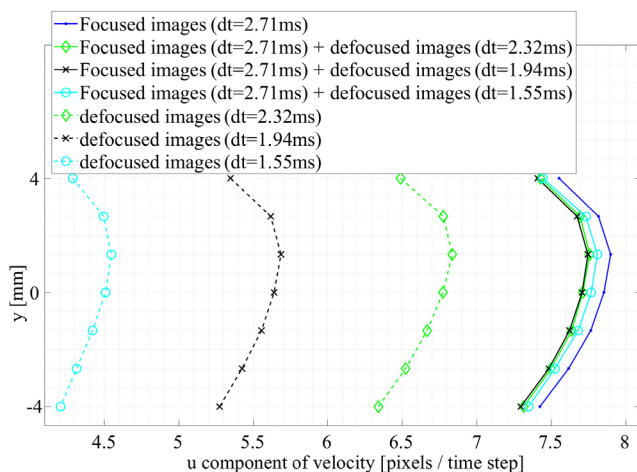


FIG. 11. The average flow profiles of region 1 of the reflected-side image. The defocused images were taken with a 15 mm plane separation. Note that the two-plane measurement error first increases and then reduces as the difference between the correct velocity and the wrong velocity increases.

experiment, the minimum plane separation can be determined based on the requirement of measurement accuracy. It is also noted that, if the flow field being measured is known *a priori*, a smaller plane separation might be achievable, because the two-plane crosstalk is affected by the flow conditions on the two planes. For example, the measurement error of the vertical velocity component is smaller, which is beneficial for measuring a flow, which is dominantly flowing vertically. We would also like to point out that, if the measurement is performed with separate cameras instead of using a single beam-split camera, the differences of the uncertainties for the two velocity components could be avoided.

Now if we look back to case 1. Consider a case 1 crosstalk with peak distance smaller than 1 pixel, the bias error caused by case 1 can be estimated as smaller than “1 pixel multiplied by the weighting function.” Referring to Fig. 8, the largest local weighting function of the 15 mm plane separation is less than 0.2. Then, the maximum bias error caused by case 1 for 15 mm plane separation can be estimated as $< (1 \text{ pixel} \times 0.2)$. This estimate lies within the bias error range indicated by Figs. 12 and 13, which are for the case 3 crosstalk. The same method could also be applied to 20 mm plane separation, for an estimation of the bias error caused by case 1 crosstalk.

4. Effect of high-pass filtering

It was mentioned in Sec. III C 2 that a high-pass filter is able to suppress the influence of bright out-of-focus particles, therefore reducing the outlier occurrence. Here, the effect of high-pass filtering on the correlation peak shape change (i.e., sub-pixel displacement estimation) is presented. For details of the high-pass filter, see Sec. III C 2. We use the same test points as in Fig. 12 and plot the average measurement errors of the horizontal velocity component in Fig. 14, as an example. At 15 mm plane separation, the average measurement error is now reduced to be smaller than 0.1 pixels per time step. The high-pass filter has a similar effect on the vertical velocity component as well, and it is not presented here. Based on the above, a high-pass filter is able to reduce case 3 crosstalk (i.e., measurement uncertainty in terms of sub-pixel displacement estimation). In future, the effect of different image filters and optimal parameters will be further investigated.

D. Summary and discussion

A laminar flow rig test was set up for an analysis of crosstalk caused by defocused particles. Each side of the split images has a $35 \times 54 \text{ mm}^2$ field of view. The three types of measurement crosstalk observed are summarized as follows: case 1: when the correct correlation peak and the wrong correlation peak are close to each other, they merge into a combined peak. In this case, the relative contribution of the defocused particles on the measured velocity can be estimated by the curvature of the correlation peak they produce. Case 2: when bright out-of-focus particles exist due to reasons such as non-uniform particle sizes, the wrong correlation peak can be higher than the correct one, resulting in the conventional “highest peak” search routine picking up the wrong peak. A sharp peak search routine is proposed here to effectively prevent such outliers. Case 3: due to the existence of the wrong correlation signal, the shape of the correct peak is inevitably changed, leading to uncertainty in terms of the sub-pixel displacement estimation.

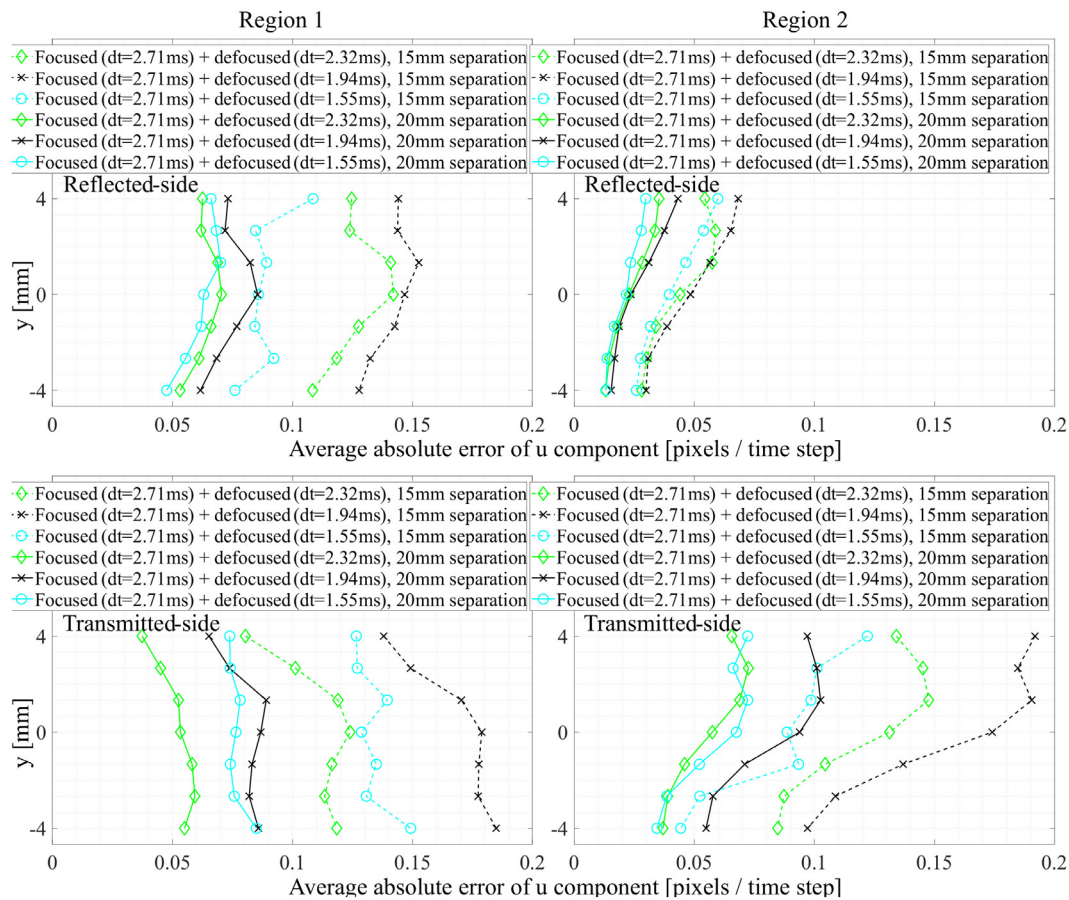


FIG. 12. The average absolute errors of the horizontal velocity component in regions 1 and 2.

The three types of crosstalk indicate that the measurement uncertainty depends not only on the extent of defocusing of the particles, but also on the flow fields. In the laminar flow test, in-focus image pairs having the same dt were numerically added with out-of-focus image pairs having different dt s, to simulate correct and wrong peaks

with different distances. With the current imaging setup, at 20 mm plane separation, the average measurement error of each velocity component is lower than 0.1 pixels per time step. It is expected that with a smaller field of view (i.e., a smaller working distance), the depth of field of the imaging system will become even more shallow, so that crosstalk

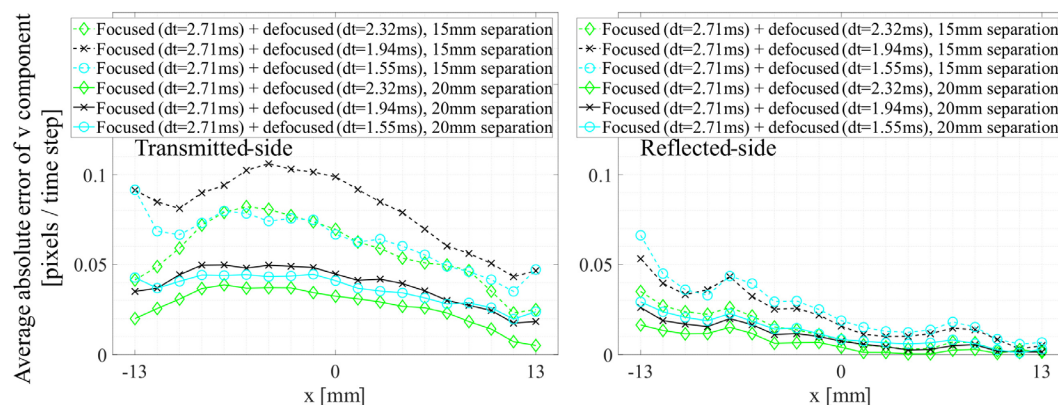


FIG. 13. The average absolute errors of the vertical velocity component in region 3.

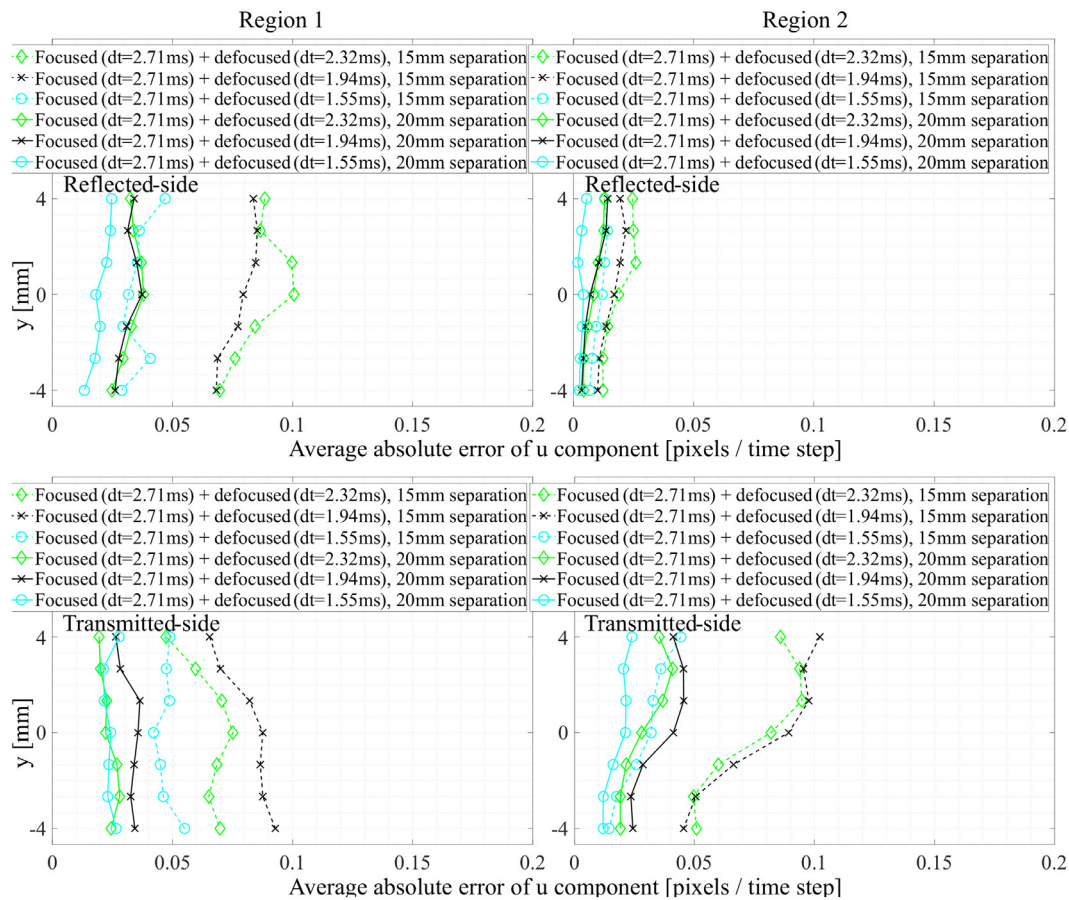


FIG. 14. The average absolute errors of the horizontal velocity component in regions 1 and 2, high-pass filtered images.

can be further reduced, and a smaller plane separation could be achieved. The effect of image pre-processing on suppressing the influence of the defocused particles has been preliminarily tested using a high-pass filter. It effectively lowers the measurement uncertainty in terms of sub-pixel estimation. The optimal filters and settings will be further investigated in future.

IV. IN-CYLINDER FLOW MEASUREMENT IN AN OPTICALLY ACCESSIBLE INTERNAL COMBUSTION ENGINE

To demonstrate the performance and robustness of the defocus-based method in a practical device where varying background scatter and out-of-plane flow motions exist, simultaneous PIV measurements on two swirl planes of an optically accessible internal combustion engine were performed.

A. Experimental setup and test condition

Measurements were performed in a single cylinder, optically accessible gasoline direct injection engine every 5°CA during the compression stroke from 120 to 55°CA before top dead center (bTDC). The engine was operated under motored conditions (Table II). A LaVision aerosol generator (the same type as used for the laminar flow

test) was used to seed olive oil droplets into the intake plenum. Figure 15 shows the experimental setup. The pair of laser beams, generated by a dual-cavity Nd:YLF laser (Photonics Industries DM20-527-DH), was split into two pairs by a 50/50 non-polarizing beam splitter cube (Edmund Optics 35959). A pair of cylindrical lenses were used to horizontally expand the laser beams. A fused silica annulus provided optical access for the laser sheets, illuminating two horizontal swirl planes of the engine. The upper plane was parallel to and 2.5 mm below the firing deck. The lower plane was 22 mm below the upper plane.

TABLE II. Engine specifications.

Bore	85 mm
Stroke	90 mm
Valves per cylinder	Two intake and two exhaust
Engine speed	1000 revolutions per minute (rpm)
Intake pressure	70 kPa
Intake air temperature	316 K
Coolant temperature	296 K
Intake air volume flow rate	1.65 l/s

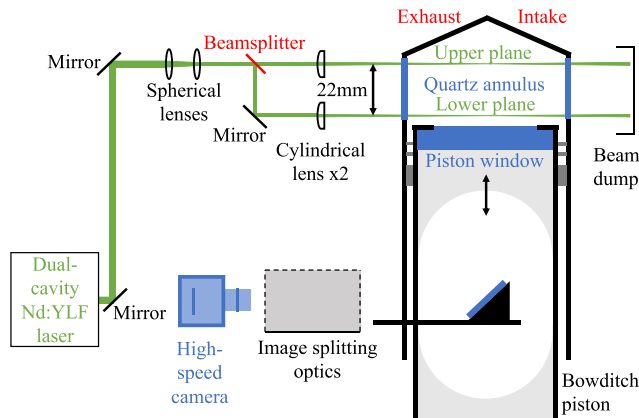


FIG. 15. Experimental setup of the engine flow measurement.

A Bowditch piston and 45° mirror arrangement enabled the swirl planes to be imaged through the piston crown window onto a high-speed CMOS camera (Phantom VEO 710L). The camera lens was the same type ($f = 85$ mm, $f/2$) as used for the laminar flow test.

Figure 16 shows an example of the simultaneous two-plane PIV raw images. Due to the existence of the strong and varying background scatter from the reflective inner surface of the cylinder head, a dynamic background subtraction filter was applied: each raw image was subtracted by the average of a summation of images, which are at the same crank angle, but from 11 consecutive cycles, including itself. The flow velocities in the central 20×18 mm² regions of the two swirl planes were calculated. Details of the PIV vector calculation routine are given in Sec. III. The interrogation windows decreased from 64×64 pixels to 32×32 pixels with a 50% overlap, leading to a vector spacing of 2.2 mm.

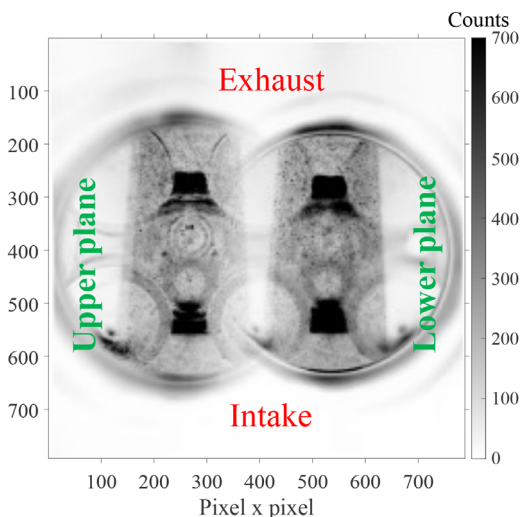


FIG. 16. An example of the simultaneous two-plane PIV raw images (black and white inverted).

Previous single-plane PIV work with the optical engine showed that, during the compression stroke, a tumble motion with an axis of rotation approximately parallel to the crankshaft would arise.¹⁹ In this section, the two-plane flow fields at 115, 80, and 65° CA bTDC are investigated, to look into the different flow conditions on the pair of swirl planes as the piston rises.

B. Measurement uncertainty analysis

In order to evaluate the measurement uncertainty caused by the out-of-focus particles, additional single-plane PIV measurements at the same test condition were performed. For clarity, we use “simultaneous two-plane test” to describe the test in which both the upper plane and the lower plane were simultaneously illuminated; “upper-plane test” for the test in which only the upper plane was illuminated; “lower-plane test” for the test in which only the lower plane was illuminated. For each test, 450 cycles of data are analyzed. By numerically adding images from the upper-plane test with the images from the lower-plane test, the measurement crosstalk is quantified. As discussed in Sec. III, the distance between the correct and the wrong correlation peaks has an influence on the exact measurement error and this is measured with the unit of pixels. Therefore, the velocity unit used in the measurement uncertainty analysis is “pixels/dt.” Real velocity values in m/s will be used for the discussion of the instantaneous flow structures of the engine.

A vector validation process was applied to all PIV vector fields. Each vector was compared to the median of its surrounding vectors. If the difference in any component of a vector was larger than 1 pixel/dt, that vector was considered spurious and replaced by the median of its surrounding vectors. Image pairs in which adjacent spurious vectors exist were discarded, so that image pairs with strong loss-of-correlation or occasional laser missynchronization were excluded. That led to about 250 usable image pairs at 115° CA bTDC, while more than 400 image pairs were usable at the other two crank angles, respectively, which indicates that a stronger out-of-plane flow motion should exist at 115° CA bTDC.

The PIV measurement results of the numerically added images are compared against the results of the single-plane images. As shown in Fig. 17, the measurement error at 115° CA bTDC is obviously larger than the errors at the other two crank angles. At 115° CA bTDC, less than 7% of all vectors have an absolute error of either component larger than 0.2 pixels/dt. At 80° CA bTDC, less than 2% of all vectors have an absolute error of either component larger than 0.2 pixels/dt. At 65° CA bTDC, less than 3% of all vectors have an absolute error of either component larger than 0.2 pixels/dt. It indicates that more measurement outliers appear at 115° CA bTDC, where a stronger out-of-plane flow motion may exist.

The absolute errors of all vectors on the upper plane at 115° CA bTDC and 80° CA bTDC are shown as scatter plots in Fig. 18. The cross (red) markers indicate the vectors located at the edges of the vector fields. The dot (blue) markers indicate the rest of the vectors. The plots show that at both 115° CA bTDC and 80° CA bTDC, the vectors at the edges of the vector fields tend to have larger errors. It should be because the PIV algorithm cannot search for matched particles outside the interrogation area, contributing to loss-of-correlation. In future work, a detailed parametric study on the influence of the PIV recording parameters (including particle loss of correlations, seeding density, etc.) on the measurement uncertainty will provide more insights.

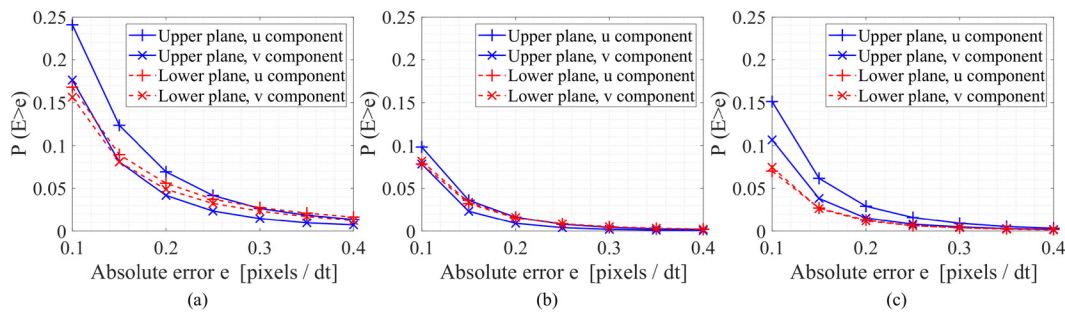


FIG. 17. The complementary cumulative distribution function of vector error E at: (a) 115°CA bTDC; (b) 80°CA bTDC; and (c) 65°CA bTDC. Note that the error at 115°CA bTDC is larger than the errors at the other two crank angles.

C. Instantaneous flow measurement on the two planes

Figure 19 shows the ensemble average flow fields on the upper plane and the lower plane in the simultaneous two-plane test. The origin (0,0) is the center of the swirl plane. Since the velocity magnitudes differ greatly for different crank angles and planes, the color maps do not readily indicate the detail of the velocity magnitudes. The overlaid vector arrows share the same scale, for a more convenient comparison.

From the average fields, it can be seen that when the piston is low (115°CA bTDC), the tumble vortex center is below the lower plane, so that the average flow direction on both planes is from the intake valves to the exhaust valves. As the piston rises to 80°CA bTDC, the vortex center has traveled across the lower plane. When the piston is higher (65°CA bTDC), the vortex center is in the middle of the two planes, so that the two planes have opposite average flow directions. However, the magnitudes of the average velocities on the lower plane at both 115°CA bTDC and 80°CA bTDC are low. Due to cyclic variation, the tumble vortex center may be at a different height in each individual cycle, even at the same crank angle. The average flow fields conceal whether the low velocity magnitudes are due to flow physics, or the varying flow motions in each individual cycle being averaged.

Figures 20 and 21 show the instantaneous flow fields from two individual cycles. In cycle A at 115°CA bTDC, the tumble vortex center lies below the two planes. At 80°CA bTDC, the vortex center aligns with the lower plane. However, in cycle B at 115°CA bTDC, the flow direction on the lower plane has already started to reverse. The two-plane PIV measurement enables the instantaneous flow structures on two planes to be measured simultaneously.

V. CONCLUSION

A multi-plane PIV method based on image splitting and defocusing has been proposed. It is an inexpensive approach that can be used alone or combined with the existing polarization/wavelength methods, so that the number of measurement plane(s) of single/multi-plane PIV setups can be increased. The method places images from two parallel planes offset in depth onto the two halves of a camera sensor, with each half focused to a different plane. Determined by the working principle, the limitations of the proposed technique include a limited field of view size (dependent on the mirror paths), minimum plane separation between the measurement planes, and reduction of the scattered light intensity by a factor of 2. The measurement uncertainty caused by the overlying image from the out-of-focus plane has been examined based on PIV cross-correlation theory and PIV

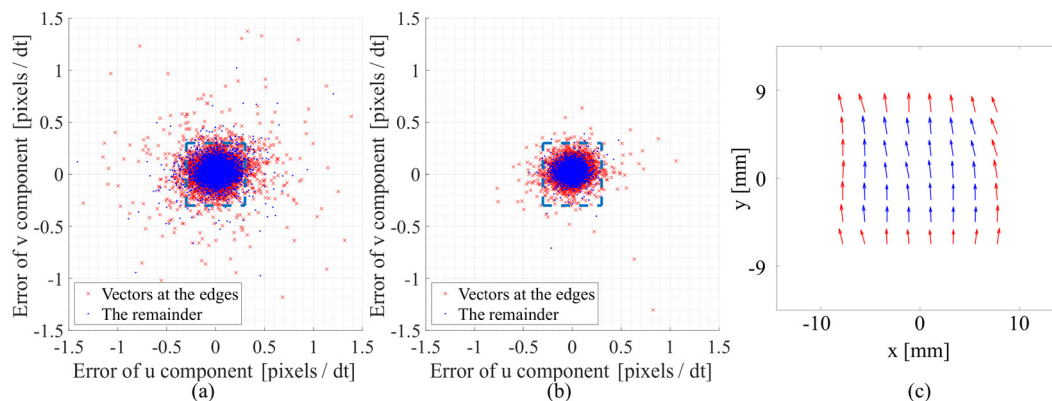


FIG. 18. Scatter plots of the absolute errors of all vectors on the upper plane at: (a) 115°CA bTDC; (b) 80°CA bTDC. Each marker corresponds to one vector. The dash boxes mark errors within ± 0.3 pixels/dt. The cross (red) markers indicate the vectors located at the edges of the vector fields; the dot (blue) markers indicate the rest of the vectors, as illustrated in (c). Note that the vectors at the edges of the vector fields tend to have larger errors.

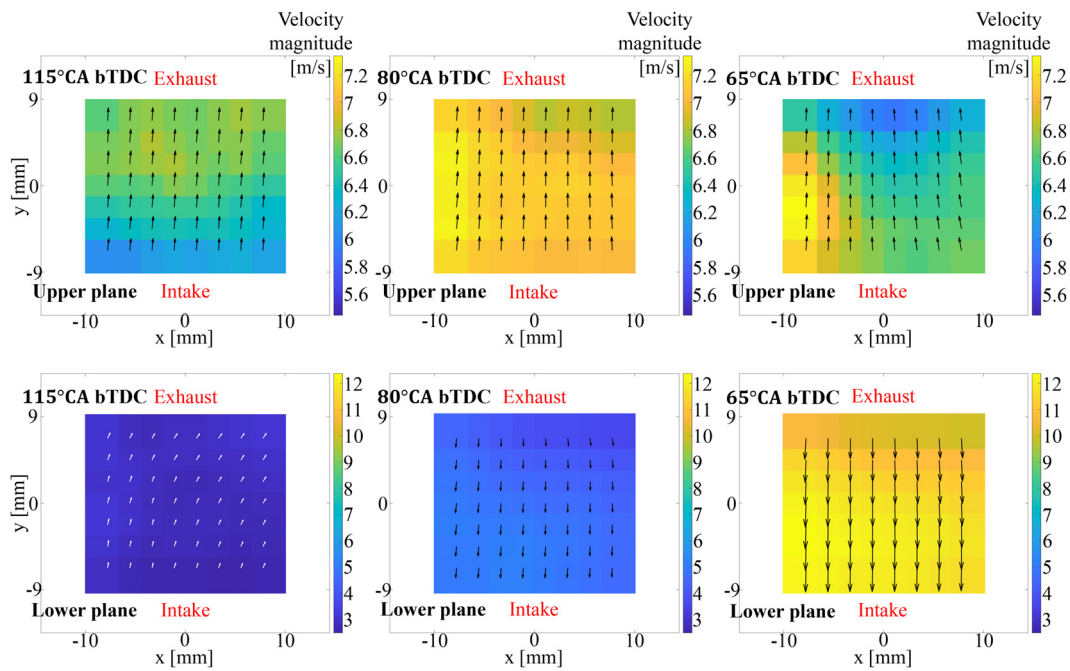


FIG. 19. The ensemble average velocity fields. The vectors have the same scale for each image. At 115°CA bTDC, the average flow direction on both planes is from the intake to the exhaust valves. At 80°CA and 65°CA bTDC, the two planes have opposite average flow directions.

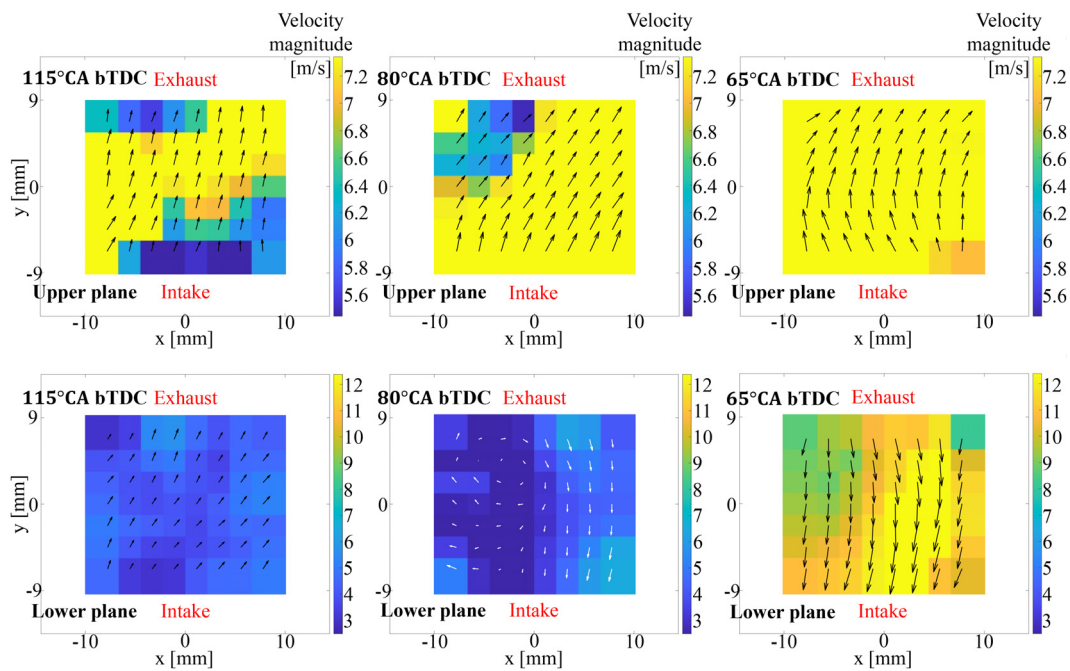


FIG. 20. The instantaneous velocity fields of cycle A. At 115°CA bTDC, the tumble vortex center is below the lower plane. At 80°CA bTDC, the tumble vortex center aligns with the lower plane.

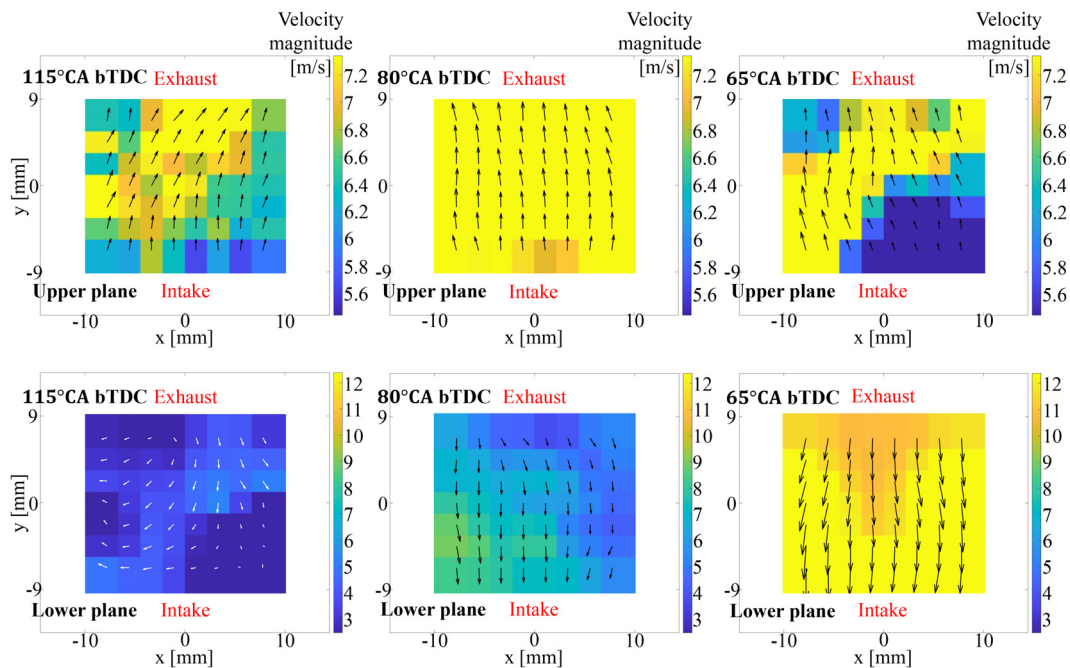


FIG. 21. The instantaneous velocity fields of cycle B. At 115°CA bTDC, the tumble vortex center has traveled across the lower plane.

measurement results from a laminar flow rig test. The latter indicates that the average measurement error of each velocity component is lower than 0.1 pixels per time step, with a 20 mm plane separation and a $35 \times 54 \text{ mm}^2$ field of view on each plane. To show its applicability, the method was employed to measure the in-cylinder flow of an optically accessible internal combustion engine, in which strong and varying background scatter and out-of-plane flow motions also interfere. PIV measurements on two swirl planes, which are 22 mm apart, were simultaneously performed.

To capitalize on the potential of the technique, further work is needed. Two-plane stereoscopic PIV based on image splitting and defocusing should be the next step. Also, the effects of different image pre-processing methods on suppressing the out-of-focus particles are worth investigating. A detailed parametric study on the influence of the PIV recording parameters (e.g., seeding density, interrogation window size, speckle and multi-scattering particularly for closely spaced sheets, correlation peak widening effect due to in-plane/out-of-plane flow gradients) on the crosstalk is also warranted. The optical characteristics of the split images may be further optimized, for example, by using different camera lenses and optics, to examine the influence of optical aberrations.

ACKNOWLEDGMENTS

This research was funded in whole or in part by an Engineering and Physical Sciences Research Council Prosperity Partnership, Grant No. EP/T005327/1. The Prosperity Partnership is a collaboration between Jaguar Land Rover, Siemens Digital Industries Software, the University of Bath and the University of Oxford. The authors thank Jesus College for supporting the

purchase of the Imperx CCD camera. Qichi He also thanks Kharthik Chakravarthy, David Ilsley, and Li Shen for their help in construction of the experimental setup.

AUTHOR DECLARATIONS

Conflict of Interest

The authors have no conflicts to disclose.

Author Contributions

Qichi He: Conceptualization (lead); Data curation (lead); Formal analysis (lead); Investigation (lead); Methodology (lead); Writing – original draft (lead); Writing – review & editing (equal). **Christopher Willman:** Investigation (equal); Methodology (equal); Writing – review & editing (equal). **Richard Stone:** Funding acquisition (equal); Resources (equal); Writing – review & editing (equal). **Benjamin Williams:** Funding acquisition (lead); Methodology (supporting); Resources (lead); Writing – review & editing (lead).

DATA AVAILABILITY

The data that support the findings of this study are openly available in Oxford University Research Archive at <http://dx.doi.org/10.5287/ora-xqv18vnrnx>, Ref. 20.

REFERENCES

- ¹A. Schröder and C. E. Willert, *Particle Image Velocimetry: New Developments and Recent Applications* (Springer Science & Business Media, 2008).
- ²A. K. Prasad, "Stereoscopic particle image velocimetry," *Exp. Fluids* **29**, 103–116 (2000).

- ³M. E. Negretti, F. L. Tucciarone, and A. Wirth, "Intruding gravity currents and re-circulation in a rotating frame: Laboratory experiments," *Phys. Fluids* **33**, 096607 (2021).
- ⁴N. Ali and A. Tariq, "Laminar and turbulent flow development study in a rectangular duct with 180° sharp bend by using stereo particle image velocimetry and liquid crystal thermography measurements," *Phys. Fluids* **35**, 015110 (2023).
- ⁵J. Bode, J. Schorr, C. Krüger, A. Dreizler, and B. Böhm, "Influence of the in-cylinder flow on cycle-to-cycle variations in lean combustion DISI engines measured by high-speed scanning-PIV," *Proc. Combust. Inst.* **37**, 4929–4936 (2019).
- ⁶F. Scarano, "Tomographic PIV: Principles and practice," *Meas. Sci. Technol.* **24**, 012001 (2013).
- ⁷X. Han, Y. Zhou, J. Li, Y. Zheng, and A. Rinoshika, "Dynamics of three-dimensional vortical structures behind a barchan dune based on tomographic particle image velocimetry," *Phys. Fluids* **34**, 075123 (2022).
- ⁸J. A. Mullin and W. J. Dahm, "Dual-plane stereo particle image velocimetry measurements of velocity gradient tensor fields in turbulent shear flow. I. Accuracy assessments," *Phys. Fluids* **18**, 035101 (2006).
- ⁹C. J. Kähler and J. Kompenhans, "Fundamentals of multiple plane stereo particle image velocimetry," *Exp. Fluids* **29**, S070–S077 (2000).
- ¹⁰Y. Naka, K. Tomita, M. Shimura, N. Fukushima, M. Tanahashi, and T. Miyauchi, "Quad-plane stereoscopic PIV for fine-scale structure measurements in turbulence," *Exp. Fluids* **57**, 63 (2016).
- ¹¹D. Dabiri and C. Pecora, *Particle Tracking Velocimetry* (IOP Publishing, Bristol, 2020), Vol. 785.
- ¹²A. Schröder and D. Schanz, "3D Lagrangian particle tracking in fluid mechanics," *Annu. Rev. Fluid Mech.* **55**, 511 (2023).
- ¹³M. Olsen and R. Adrian, "Out-of-focus effects on particle image visibility and correlation in microscopic particle image velocimetry," *Exp. Fluids* **29**, S166–S174 (2000).
- ¹⁴M. Rossi, R. Segura, C. Cierpka, and C. J. Kähler, "On the effect of particle image intensity and image preprocessing on the depth of correlation in micro-PIV," *Exp. Fluids* **52**, 1063–1075 (2012).
- ¹⁵M. G. Olsen, "Directional dependence of depth of correlation due to in-plane fluid shear in microscopic particle image velocimetry," *Meas. Sci. Technol.* **20**, 015402 (2009).
- ¹⁶M. G. Olsen, "Depth of correlation reduction due to out-of-plane shear in microscopic particle image velocimetry," *Meas. Sci. Technol.* **21**, 105406 (2010).
- ¹⁷W. Thielicke and E. Stamhuis, "PIVlab—Towards user-friendly, affordable and accurate digital particle image velocimetry in MATLAB," *J. Open Res. Software* **2**, e30 (2014).
- ¹⁸C. J. Bourdon, M. G. Olsen, and A. D. Gorby, "Validation of an analytical solution for depth of correlation in microscopic particle image velocimetry," *Meas. Sci. Technol.* **15**, 318 (2004).
- ¹⁹L. Shen, C. Willman, R. Stone, T. Lockyer, R. Magnanon, and G. Virelli, "Multi-plane PIV measurements in a gasoline direct injection engine," *SAE Int. J. Adv. Curr. Pract. Mobility* **3**, 223 (2020).
- ²⁰Q. He, C. Willman, R. Stone, and B. A. O. Williams (2023). "Inexpensive multi-plane particle image velocimetry based on defocusing: Proof of concept on two-component measurement," *University of Oxford*. <http://dx.doi.org/10.5287/ora-xqv18vnrx>